



The dynamics of SARS-CoV-2 infectivity with changes in aerosol microenvironment

Henry P. Oswin^a, Allen E. Haddrell^{a,1}, Mara Otero-Fernandez^a, Jamie F. S. Mann^b, Tristan A. Cogan^b, Thomas G. Hilditch^a, Jianghan Tian^a, Daniel A. Hardy^a, Darryl J. Hill^c, Adam Finn^c, Andrew D. Davidson^{c,1}, and Jonathan P. Reid^{a,1}

Edited by Michael Oldstone, The Scripps Research Institute, La Jolla, CA; received January 6, 2022; accepted April 28, 2022

Understanding the factors that influence the airborne survival of viruses such as severe acute respiratory syndrome coronavirus 2 (SARS-CoV-2) in aerosols is important for identifying routes of transmission and the value of various mitigation strategies for preventing transmission. We present measurements of the stability of SARS-CoV-2 in aerosol droplets (~ 5 to $10 \mu\text{m}$ equilibrated radius) over timescales spanning 5 s to 20 min using an instrument to probe survival in a small population of droplets (typically 5 to 10) containing ~ 1 virus/droplet. Measurements of airborne infectivity change are coupled with a detailed physicochemical analysis of the airborne droplets containing the virus. A decrease in infectivity to $\sim 10\%$ of the starting value was observable for SARS-CoV-2 over 20 min, with a large proportion of the loss occurring within the first 5 min after aerosolization. The initial rate of infectivity loss was found to correlate with physical transformation of the equilibrating droplet; salts within the droplets crystallize at relative humidities (RHs) below 50%, leading to a near-instant loss of infectivity in 50 to 60% of the virus. However, at 90% RH, the droplet remains homogenous and aqueous, and the viral stability is sustained for the first 2 min, beyond which it decays to only 10% remaining infectious after 10 min. The loss of infectivity at high RH is consistent with an elevation in the pH of the droplets, caused by volatilization of CO_2 from bicarbonate buffer within the droplet. Four different variants of SARS-CoV-2 were compared and found to have a similar degree of airborne stability at both high and low RH.

aerosol | SARS-CoV-2 | airborne transmission | microphysics | environmental conditions

The ongoing coronavirus disease 2019 (COVID-19) pandemic has demonstrated the requirement for an improved understanding of the factors that govern the relative importance of different modes of transmission of respiratory pathogens, including the parameters that influence droplet, fomite, and airborne transmission. Indeed, shortcomings in our understanding have prolonged the debate surrounding the likelihood of airborne transmission of severe acute respiratory syndrome coronavirus 2 (SARS-CoV-2) (1–3), with consequences for the implementation of nonpharmaceutical interventions and mitigation strategies such as physical distancing, the wearing of face coverings, and the use of ultraviolet (UV) germicidal irradiation. Currently, epidemiological evidence (4–7), air sampling studies (8), and animal-model studies (9) are broadly consistent with transmission dominated by the inhalation of infectious aerosol ($<100\text{-}\mu\text{m}$ diameter). Transmission over distances beyond 2 m has been documented and tends to be under preventable circumstances (10), such as occurring after prolonged exposure in poorly ventilated rooms (11, 12).

Reports of the airborne stability of SARS-CoV-2 consistently indicate that the half-life associated with the decay in viral infectivity is on the order of hours in surrogates of respiratory aerosols (13–16). However, a detailed understanding of the processes that govern the airborne longevity of viruses, and how infectivity is affected by basic environmental conditions such as relative humidity (RH) and temperature, is required. More specifically, there is little clarity on the impact of environmental conditions on the microenvironment within an airborne droplet and the interplay between this microenvironment and the stability of pathogens. Improved models of the physicochemical properties of respiratory aerosol and the processes that transform particle size, moisture content, composition, and phase are essential to provide clearer insights into the relative risks of airborne transmission in different environments and the potential benefits of mitigation measures to reduce transmission. Indeed, it should be recognized that transformation processes lead to transient changes in properties (e.g., surface enrichment in salts during evaporation following droplet exhalation) that can have impacts on infectivity distinct from the steady state equilibrium properties that persist

Significance

The aerosol microenvironment is dynamic, exposing pathogens, such as severe acute respiratory syndrome coronavirus 2 virus, when exhaled in respiratory aerosol to extreme conditions of solute concentration, pH, and evaporative cooling. Yet surviving this environment is a key step in the transmission of such pathogens. Understanding the impact that airborne transport has on pathogens and the influence of environmental conditions on pathogen survival can inform the implementation of strategies to mitigate the spread of diseases such as coronavirus disease 2019. We report changes in the infectivity of the airborne virus over timescales from 5 s to 20 min and demonstrate the role of two microphysical processes in this infectivity loss, namely, particle crystallization and aerosol droplet pH change.

Author affiliations: ^aSchool of Chemistry, Cantock's Close, University of Bristol, Bristol BS8 1TS, United Kingdom; ^bBristol Veterinary School, University of Bristol, Langford, Bristol BS40 5DU, United Kingdom; and ^cSchool of Cellular and Molecular Medicine, University of Bristol, Bristol BS8 1TS, United Kingdom

Author contributions: H.P.O., A.E.H., J.F.S.M., D.J.H., A.F., A.D.D., and J.P.R. designed research; H.P.O., A.E.H., M.O.-F., T.A.C., T.G.H., J.T., and D.A.H. performed research; T.A.C. and A.D.D. contributed new reagents/analytic tools; H.P.O., A.E.H., M.O.-F., T.A.C., T.G.H., J.T., D.A.H., and J.P.R. analyzed data; H.P.O., A.E.H., J.F.S.M., D.J.H., A.F., A.D.D., and J.P.R. wrote the paper.

The authors declare no competing interest.

This article is a PNAS Direct Submission.

Copyright © 2022 the Author(s). Published by PNAS. This open access article is distributed under Creative Commons Attribution License 4.0 (CC BY).

¹To whom correspondence may be addressed. Email: A.Haddrell@bristol.ac.uk, Andrew.Davidson@bristol.ac.uk, or j.p.reid@bristol.ac.uk.

This article contains supporting information online at <http://www.pnas.org/lookup/suppl/doi:10.1073/pnas.2200109119/-DCSupplemental>.

Published June 28, 2022.

over longer time periods during airborne transport (e.g., an equilibrated salt concentration).

The microenvironment within an airborne droplet is multifarious and notoriously difficult to study (17) and is further complicated by the presence of organic macromolecules and microorganisms (18). While the vast majority of indoor aerosols originate from sources such as candles, dust, outdoor air pollution, and food cookers (19), respiratory pathogens are transmitted in exhaled aerosol that can span from 100-nm to 100- μm diameter and have emission rates as low as 10 particles s^{-1} when humans breathe (20, 21). Regardless of the expiratory activity that generates respiratory aerosols [e.g., coughing, speaking (21, 22)], the high surface area-to-volume ratio of the emitted particles facilitates rapid equilibration to the surrounding gas phase composition (*SI Appendix, Fig. S1A*) (23). In particular, the equilibration of the water activity within the droplet to the surrounding RH impacts the physicochemical conditions experienced by microorganisms present within the aerosol. Aqueous respiratory droplets at the point of exhalation start with a very high water activity (~ 0.995) (24) consistent with equilibration with the high RH within the respiratory tract (25) but must adjust to equilibrate with the indoor humidity, which is typically within the range 20 to 60% (26–28). Under most conditions, exhaled aerosol droplets rapidly lose both moisture and heat through evaporation, with large concomitant changes in volume and temperature as they establish an equilibrium with the indoor environment.

Not only does the loss in water lead to an increase in solute concentrations during evaporation but also the absence of heterogeneous nucleation sites (i.e., a surface) leads to supersaturated solute concentrations that cannot be achieved in the bulk solution phase or in sessile droplets deposited on surfaces. At sufficiently low RH (e.g., below 45% for saline solution droplets), the supersaturation of solutes can be sufficient to induce homogenous nucleation (29–31) of the salt fraction, leading to efflorescence (crystallization) of the droplet and the formation of a dryer particle. Furthermore, during the initial period of droplet evaporation, the rates of diffusion of microorganisms within the droplet can be significantly slower than the rate at which the droplet surface recedes, leading to their exclusion to the near-surface region of the droplet. Given that the physicochemical conditions at the surface of the droplet can be different to the core (e.g., surface enrichment in solute concentration), establishing the distribution of microorganisms within a particle may be crucial to understanding the impact of aerosol microphysics on their longevity.

Once the moisture content of the aerosol has decreased to establish equilibrium with the ambient environment, the decay in microorganism survival may be regulated by steady-state microphysical properties. In particular, the typical range in ambient RH is consistent with equilibrated solute concentrations that are supersaturated in the exhaled aerosol. Although the mechanism remains unclear, high salt concentrations may inactivate viruses by damaging the viral nucleic acid (32, 33). With high contents of organic macromolecules, phase-separated particles with organic- and inorganic-rich domains or amorphous particles containing trapped moisture may form, potentially enhancing viral and bacterial survival. Furthermore, the pH of aerosol particles is RH, size, and composition dependent, and the pH of aerosol droplet surfaces may be different from the droplet bulk (34). Indeed, predicting the evolving aerosol pH is challenging, particularly when the facile partitioning of water-soluble acidic and basic components from the ambient environment is considered, even before the influence of aerosol pH on microorganism survival is considered (35).

Laboratory strategies to assess the airborne stability of a pathogen must either be capable of simulating every aspect of the real-world environment in which transmission occurs or sufficient control over the conditions must be achieved such that the influence of individual processes and properties on survival can be assessed independently. Goldberg rotating drums (36) have been widely used over many decades to assess airborne pathogen stability and have been used to investigate the airborne survival of SARS-CoV-2. More specifically, studies have examined the dependence of infectivity on time (20 min to 16 h), RH (40 to 70%), and the presence of UVC light with measurements in aerosols composed of cell culture media (Dulbecco's modified Eagle medium [DMEM] and minimal essential media [MEM]) and artificial saliva (13–16, 37). All studies concentrate on equilibrated particle sizes of $\sim 5 \mu\text{m}$ (mass median aerodynamic diameter). A nebulizer is used to generate a cloud of aerosolized pathogen that is suspended by the rotation of the drum. The initial environmental conditions within the drum can be controlled by mixing the output of the nebulizer with a flow of humidity- and temperature-controlled air. However, operation with stable environmental conditions can be challenging; for example, as the droplets evaporate and equilibrate to the set humidity, the water they release can cause the humidity within the drum to increase [see for example the report of Smither et al. (14)]. In addition, dynamic changes in liquid water content within the freshly nebulized aerosol cloud do not replicate the very rapid changes that can accompany the extremely low concentrations of the exhaled aerosol. This precludes any study of short-term decreases in pathogen viability that may be critical to understanding close contact transmission and the immediate consequences of exhalation on microbe survival.

We have previously reported a unique approach to the study of infectious aerosol and the interplay between aerosol microphysics and pathogen survival, using complementary aerosol analysis techniques to assess the underlying mechanisms that govern the airborne longevity of pathogens (38, 39). The aerosol stability of viruses and bacteria is investigated using the CELEBS (controlled electrodynamic levitation and extraction of bioaerosols onto a substrate) technique (38–40). In CELEBS (*SI Appendix, Fig. S1B*), a small population (< 20) of near-identical monodisperse droplets containing bacteria or viruses are trapped within an electric field, while a constant flow of air prevents the accumulation of released water around the droplets. Loading droplets into the CELEBS takes $< 0.1 \text{ s}$, and there is no physical loss of droplets over time. Thus, an assessment of the viability of suspended microbes within droplets can be made after periods of suspension varying between less than 5 s to many hours. These longevity measurements can then be contextualized with detailed measurements of the dynamic changes in the physicochemical properties of droplets generated the exact same way in an instrument referred to as the comparative kinetic-electrodynamic balance (CK-EDB) (38, 41–45). The CK-EDB uses the same piezoelectric droplet-on-demand dispensers as the CELEBS to generate droplets, with particles captured in the path of a laser within a flow of humidity and temperature-controlled air (*SI Appendix, Fig. S1C*). The elastic light scattering pattern can be used to infer the size and structure of these droplets within the same environmental conditions as those used in CELEBS.

By coupling the time-sensitive measurements of the physicochemical properties of the droplets (CK-EDB) with the downstream biological effects (CELEBS) on the same timescale, the systematic exploration of hypotheses regarding the inactivation

mechanisms of viruses and bacteria is possible. In this study, we apply this approach to the study of SARS-CoV-2 survival in airborne droplets of cell culture medium, examining the survival over timescales spanning from <20 s, commensurate with the evaporation of freshly exhaled aerosol, through to 20 min. By studying the physicochemical changes that take place in the droplet and exploring how these changes impact the infectivity of the virus, we elucidate the effect of the airborne environment on SARS-CoV-2. This study provides insights into the potential influence of environmental conditions on COVID-19 transmission.

Results

The Airborne Infectivity of SARS-CoV-2 Declines over the First 20 min following Aerosolization. The infectivity of SARS-CoV-2 contained in droplets of MEM with 2% vol/vol fetal bovine serum (MEM 2% FBS) was measured over the course of 20 min of levitation in CELEBS at both low (40%) and high (90%) RH (Fig. 1A). A decrease in infectivity (in this work, defined as the proportion of virus remaining able to induce cytopathic effect) at low RH occurs almost immediately, falling to an average of 54% within 5 s of generation. Interestingly, although the initial loss in infectivity at low RH is almost instant, the virus infectivity then remains more stable, only decreasing an average of 19% over the next 5 min. At high RH, the reduction in infectivity following aerosolization is more gradual with a steady loss of infectivity of 48% within the first 5 min. The decay in survival appears to plateau at both RHs after 10 min, and the difference between infectivity in aerosol particles suspended at the two RHs diminishes over time, until survival at the two RHs is indistinguishable after 20 min. Further research will be required to explore for how long the apparent plateau continues, but it is possible that this slowing down of the viral decay is responsible for the longer half-lives reported in previous Goldberg rotating drum studies (15). It is unlikely that the rapid initial decay in virus infectivity

would be observable in a rotating drum due to the relatively long times required to load the drum.

To more fully characterize the dependence of the infectivity of SARS-CoV-2 on RH, the RH was varied from 30 to 90% and the infectivity remaining at 2 min measured. Previous studies have reported little dependence of the infectivity decay rate on RH within the uncertainty of the measurements (14, 16). However, we observe a clear relationship between the short-term viability of SARS-CoV-2 and RH (Fig. 1B). Between 30 and 50% RH, the infectivity typically declines within this short time frame to between 30% and 40% after 2 min of levitation. At RHs of 80% and above, the virus is far more stable, with infectivity rarely falling below 80% after 2 min. The residual infectivity between 60% and 70% RH is highly variable, sometimes falling to similar levels to those observed at the lower RHs and sometimes showing almost no decrease; we shall return to this variability in a later section.

The rapid decay in infectivity reported here, with an observed half-life of on the order of seconds to minutes, has not been reported previously. However, consistent with the majority of previous studies, these survival decays have been measured in virus culture directly and it should be remembered that the aerosol composition (MEM 2% FBS) is different from real exhaled respiratory fluids, including saliva, alveolar lung fluid, and other respiratory secretions. Thus, we now investigate the causative mechanisms driving the decay of SARS-CoV-2 in airborne MEM 2% FBS in order to better understand the relevance of these measurements to the transmission of SARS-CoV-2.

Airborne Droplets of MEM Show Complex Phase Behavior during Evaporation. To provide insight into the underlying mechanisms that drive the observed airborne loss of SARS-CoV-2 infectivity, the microphysical changes (depicted in *SI Appendix, Fig. S1A*) taking place in the droplets hosting the virus were explored in real time and in situ using the CK-EDB with a time resolution of <100 ms (38, 41–45). For context, the phase changes that occur during the evaporation of aqueous sodium chloride at an RH below the efflorescence threshold are

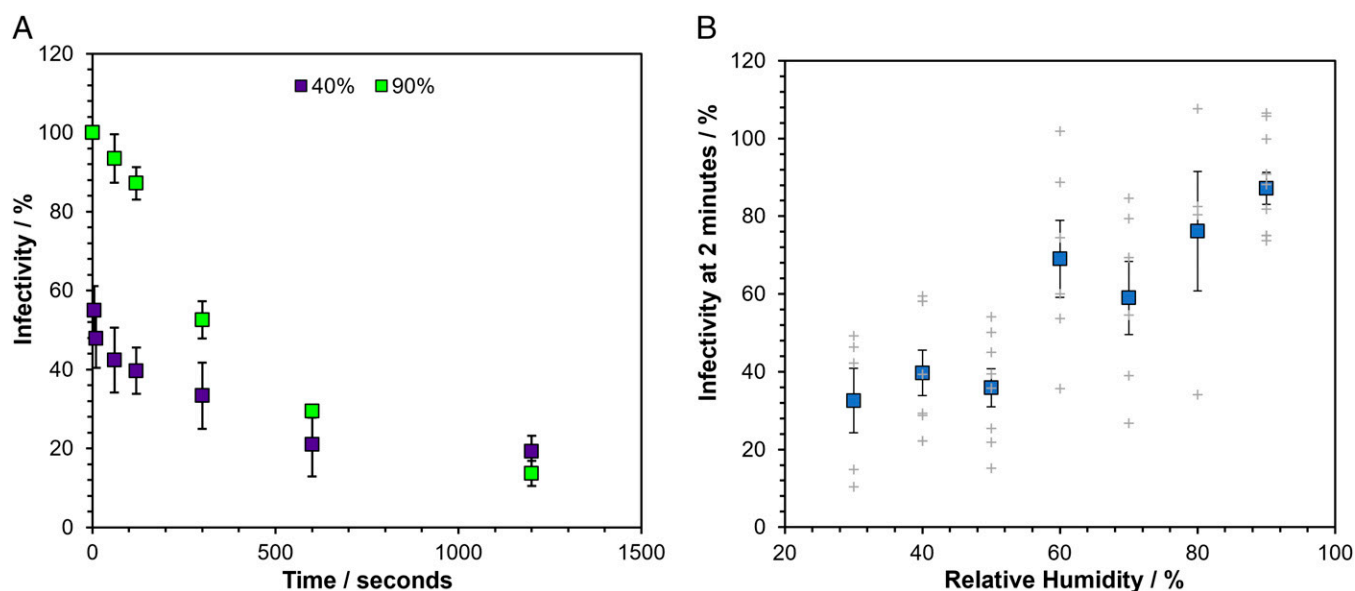


Fig. 1. The short-term airborne decay of SARS-CoV-2. Datapoints are the mean of several measurements (typically >4), and error bars show the standard error. Measurements were carried out at room temperature at 18 to 21°C. (A) The percentage infectivity of SARS-CoV-2 REMRQ0001 as a function of time levitated in CELEBS at 40% RH (purple) and 90% RH (green). (B) Curve showing the impact of RH on the percentage infectivity of SARS-CoV-2 REMRQ0001 after 2 min of levitation in CELEBS. The larger colored square points show the mean, with the error bars showing the standard error. Gray crosses show the results of individual measurements.

shown in *SI Appendix, Fig. S2*. When efflorescence occurs at low RH, the crystallization of the salt is exothermic, resulting in a transient increase in the droplet temperature and a concomitant increase in the evaporation rate. This increase in evaporation rate characteristic of efflorescence is best observed in changes in the intensity of the total light scattered by the particle. By comparison, Mie scattering calculations from the angularly resolved light scattering pattern can be used for precise estimation of the droplet size and can provide other insights into the physical transformations of the particle, such as the formation of numerous submicron crystals dispersed within the host liquid droplet and the point at which the particle ceases to be spherical (46).

For the viral longevity measurements in this study, the virus was suspended in MEM 2% FBS, which was the tissue culture medium used in the initial growth of the virus on Vero cells. The relatively low viral titers obtained with SARS-CoV-2 culture (47) prevented dilution into other solutions, constraining longevity experiments to the starting stock solution. We avoided concentrating the virus stocks using methods such as ultracentrifugation and tangential flow filtration to avoid any impact these processes might have on the stability of the virus, which could then introduce ambiguity into the interpretation of the longevity data. MEM is a complex solution containing a range of inorganic salts and organic components such as proteins, amino acids, and various sugars. The composition is made more complicated and uncertain through the addition of an animal extract (FBS). Saliva and lung fluid are also complex mixtures of inorganic and organic components, with many solutes at similar concentrations to those found in MEM. For example, MEM contains 3.3 g/L of sodium, 0.2 g/L of potassium, and 1.6 g/L of bicarbonate. For human saliva, these concentrations range from 0.26 to 5 g/L for sodium (48), 0.1 to 0.7 g/L for potassium (48), and 0.5 to 2 g/L for bicarbonate (49), putting the concentrations in MEM within the expected ranges for saliva. It should be noted though that the composition of saliva can vary

significantly from individual to individual, with sampling conditions, and over the course of a respiratory infection (50–54).

To better understand the response of aerosols, formed from the complex mixture of components typical of cell culture media and respiratory secretions, to the airborne environment, the drying kinetics of droplets containing MEM 2% FBS were studied using the CK-EDB. Evaporation curves for droplets of MEM 2% FBS levitated at a range of RHs are shown in Fig. 2*A*. From the evaporation rates reported here, it is possible to estimate that the change in droplet temperature driven by evaporative cooling will not exceed a transient reduction of 5.5 °C, which is unlikely to influence viral infectivity. At an RH of 51% and below, changes in the overall light scatter intensity typical of efflorescence were observed (*SI Appendix, Fig. S3*), with the droplets crystallizing in less than 5 s from generation. At a measurement RH of 67%, efflorescence was not observed, although the recorded Mie scattering profile indicates that the particles are no longer spherical, potentially forming inhomogeneous amorphous semisolid particles (Fig. 2*A*). Indeed, at 78% RH, variability in the outcome of the dynamics and phase transformation of the aerosol was observed; particles initially underwent a phase change (possibly with the formation of inclusions) that was sometimes reversible, reforming a homogeneous spherical particle at a later time. At RHs of 85% and above, particles mostly remained homogeneous aqueous spheres. The dependence of the apparent final particle structure on RH is summarized in Fig. 2*B*. At the extremes of RH, particles of consistent phase were formed following drying and equilibration, with crystalline or spherical homogeneous solution droplets resulting at low and high RH, respectively. At intermediate RHs, variability in the physical state of the equilibrated particle was observed, mirroring the greater variability in the remaining infectivity of SARS-CoV-2 at 2 min across these RHs (Fig. 1*B*). We shall return to a fuller explanation of the phase behavior of the droplets at these intermediate RHs in a later section.

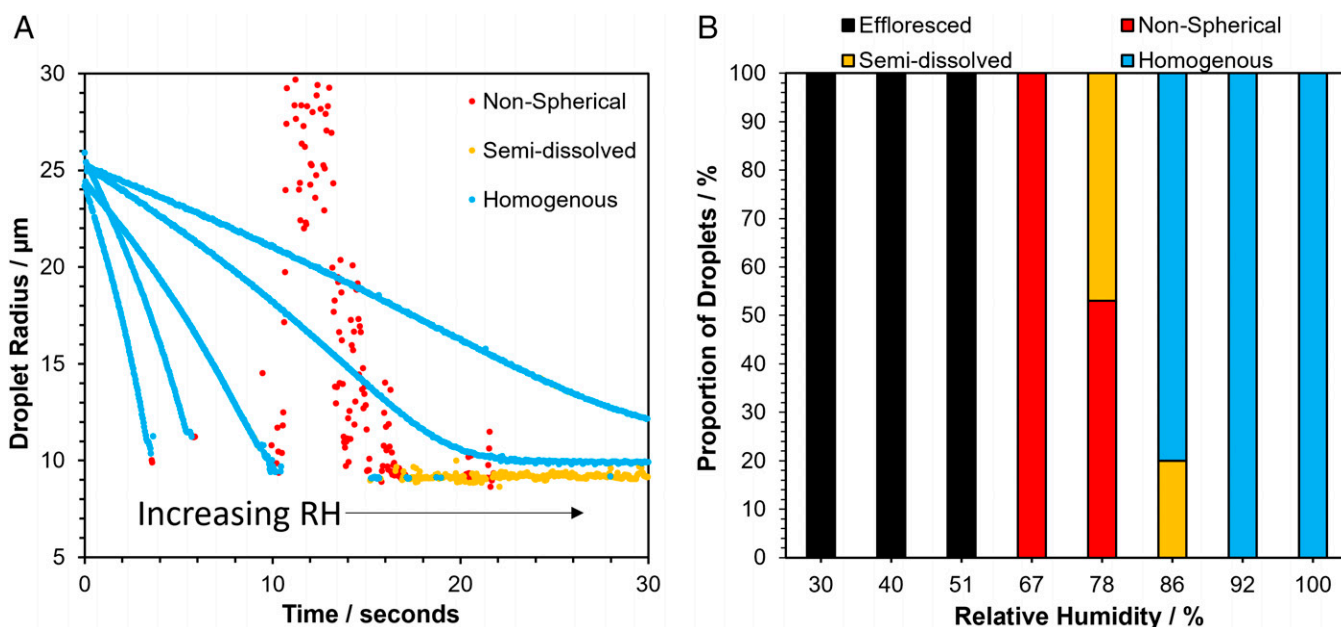


Fig. 2. The microphysics of airborne MEM droplets. (A) Mie scatter evaporation profiles of MEM 2% FBS generated by a droplet dispenser and levitated in the CK-EDB at different RHs (51, 66.8, 78.2, 86, 92, *Left to Right*). Blue indicates a homogenous spherical droplet, yellow indicates the presence of inclusions within the droplet, and red indicates a nonspherical particle (note that size estimates become inaccurate for nonspherical particles). (B) Proportion of particle morphologies formed by MEM 2% FBS at different RHs. The frequency of the formation of each particle type is shown for the RHs studied, with black indicating efflorescence, red indicating a nonspherical particle, yellow indicating a semi dissolved particle, and blue indicating an aqueous homogenous particle.

The relationships between the RH, the rate of evaporation, and the volume change during drying for aqueous MEM droplets are shown in *SI Appendix, Fig. S4*. The solute molarities increase from their initial values by around 10-fold when droplets evaporate into a gas phase at 92% RH and 25-fold at 78.2%, as reflected by the change in droplet radius and, thus, volume. Below this RH, inclusion formation (likely by some of the solute components crystallizing from solution) precludes an accurate estimation of the degree of supersaturation achieved within the remaining liquid phase. Although equilibration timescales are size dependent (smaller droplets would be expected to reach equilibrium much faster), the overall increase in solute concentration is size independent.

During equilibration to the ambient RH, the surface of an evaporating droplet can become enriched with larger solutes and suspended matter if the rate at which the surface is receding (κ , $\text{m}^2 \text{s}^{-1}$) is faster than the rate of diffusional mixing (reflected in the diffusion constant, D_i , $\text{m}^2 \text{s}^{-1}$) (55, 56). This competition is characterized by the Peclet number, Pe_i , for component i :

$$Pe_i = \frac{\kappa}{8D_i}. \quad [1]$$

By comparing the evaporation rates reported in Fig. 2A (and *SI Appendix, Fig. S4*) with the previously reported diffusion coefficient for a typical virus in water (57, 58), the Pe_i for SARS-CoV-2 in MEM 2% FBS can be estimated. In all cases and for all temperatures studied here, the initial Pe_i for SARS-CoV-2 at the starting droplet water activity can be assumed to be in the range 0.5 to 5, showing marginal surface enrichment at most (59). As the water content diminishes during evaporation, particularly when drying into low RH, the increasing solute concentrations may slow the diffusion of the virus and may lead to surface segregation, although we do not account for this here. Indeed, Pe_s for more highly diffusing solutes will be $\ll 1$ and can be assumed to show only marginal surface enrichment at the lowest RHs and highest temperatures; for example, at a Pe_i of 0.2, drying aqueous sodium chloride droplets show a transient enrichment in surface salt concentration of $\sim 20\%$ above the droplet core concentration for similarly sized droplets (60).

Efflorescence Enhances the Loss of Infectivity in Aerosol at Low RH. The loss of infectivity at low RHs appears to be consistent with observations of a change in phase state for the airborne droplet with a reproducible decrease in infectivity observed when efflorescence occurs. However, it remains unclear whether the efflorescence event itself impacts the infectivity of the virus. To confirm the correlation with phase behavior, the RH was cycled above (75% RH) and below (40% RH) the efflorescence threshold twice during a 2-min levitation (Fig. 3A). The infectivity for three out of the four levitations fell below the detection limit, indicating a $>90\%$ loss of infectivity. This loss of infectivity was far greater than during 2-min levitations where the RH was maintained at either a constant 40% RH, resulting in a single efflorescence event and an average infectivity of 40%, or at 70% RH for which no efflorescence would occur, which resulted in an average infectivity of 59%. A more detailed account of this measurement can be seen in *SI Appendix, Fig. S5*, with infectivity measured before and after each efflorescence event.

A CK-EDB measurement of a levitated MEM droplet, in which the RH was cycled between the same values as in the CELEBS survival measurement, is shown in Fig. 3B. These data confirm that a cycle of evaporation and efflorescence, redissolution, efflorescence, and redissolution occurs as the RH

is cycled between 75, 45, 75, 45, and 75%. As in previous CK-EDB measurements of MEM, the particles were predominantly aqueous at the higher RH but with some solid inclusion content. For the cycled RH measurements in Fig. 3A (and *SI Appendix, Fig. S5*), the droplets were deposited at high RH ensuring they were in a dissolved solution phase on sampling. This indicates that the efflorescence-driven loss in infectivity did not arise from a physical sequestration of the virus in non-dissolving salt crystals but reflected an infectivity impairing alteration to the virus itself.

The consistency in the infectivity reduction induced on efflorescence, even when multiple efflorescence events take place in the same droplet population, demonstrates that there is no inherent property of individual virions that protects them from the crystallization event. The factor that determines whether an individual virion retains infectivity postefflorescence must instead depend on the local conditions in the vicinity of each individual virion. It was possible to image the evaporation and efflorescence of airborne MEM 2% FBS at 40% RH using a falling droplet column (Fig. 3C). In flight, there is considerable variability in the morphology of the MEM particle immediately after crystallization, which is apparent also in the dried MEM 2% FBS droplets collected and imaged with scanning electron microscopy (SEM) (also Fig. 3C). These images of the effloresced media reveal that some of the particle is crystalline while some is not. Thus, it is possible that whether or not the virus is in the crystallized fraction of a particle determines its stability following efflorescence. Interestingly, the salt crystals formed are smaller and more numerous as the RH is lowered (*SI Appendix, Fig. S6*), consistent with previous work that has shown that there is a greater propensity for nucleation when droplets are dried at higher rates leading to more nucleation events and smaller final crystals forming a larger composite particle (61).

Changing the temperature of the air around the droplets while maintaining the RH below the efflorescence point does not significantly impact the observed loss of infectivity (Fig. 3D). This provides further evidence that the mechanism driving the loss of infectivity is a physical process such as efflorescence rather than a thermodynamically driven chemical process, such as the rate at which the solute concentrations increase during the evaporation process. The temperature change marginally alters the timepoint at which efflorescence occurs, but the droplets all effloresce within 25 s for all three temperatures reported here, well before the 5-min point at which droplets were sampled and infectivity measured.

Airborne Longevity Appears Similar for Different SARS-CoV-2 Variants. Most measurements in this study were carried out using SARS-CoV-2 isolated early in the pandemic (SARS-CoV-2/human/Liverpool/REMRQ0001/2020 [REMRQ0001]). We compared the data from this variant with CELEBS measurements with three others to determine if changes in the structure of SARS-CoV-2 could have an impact on its response to the airborne environment. At 5 min, a decrease in infectivity was observed both at 40 and 90% RH for REMRQ0001, providing the optimum time to resolve any differences in aerostability. At both 40 and 90% RH, no significant difference was observed between REMRQ0001, B.1.1.7 (the Alpha variant), a mutant of the SARS-CoV-2 isolate England/2/2020 that has the same Spike protein sequence as REMRQ0001 except that the furin cleavage site is deleted (designated BriSA) (62, 63), and B.1.351 (the Beta variant) (Fig. 4). It is possible that if this comparison is expanded to cover a broader range of times and conditions, differences between these variants will be observable. However,

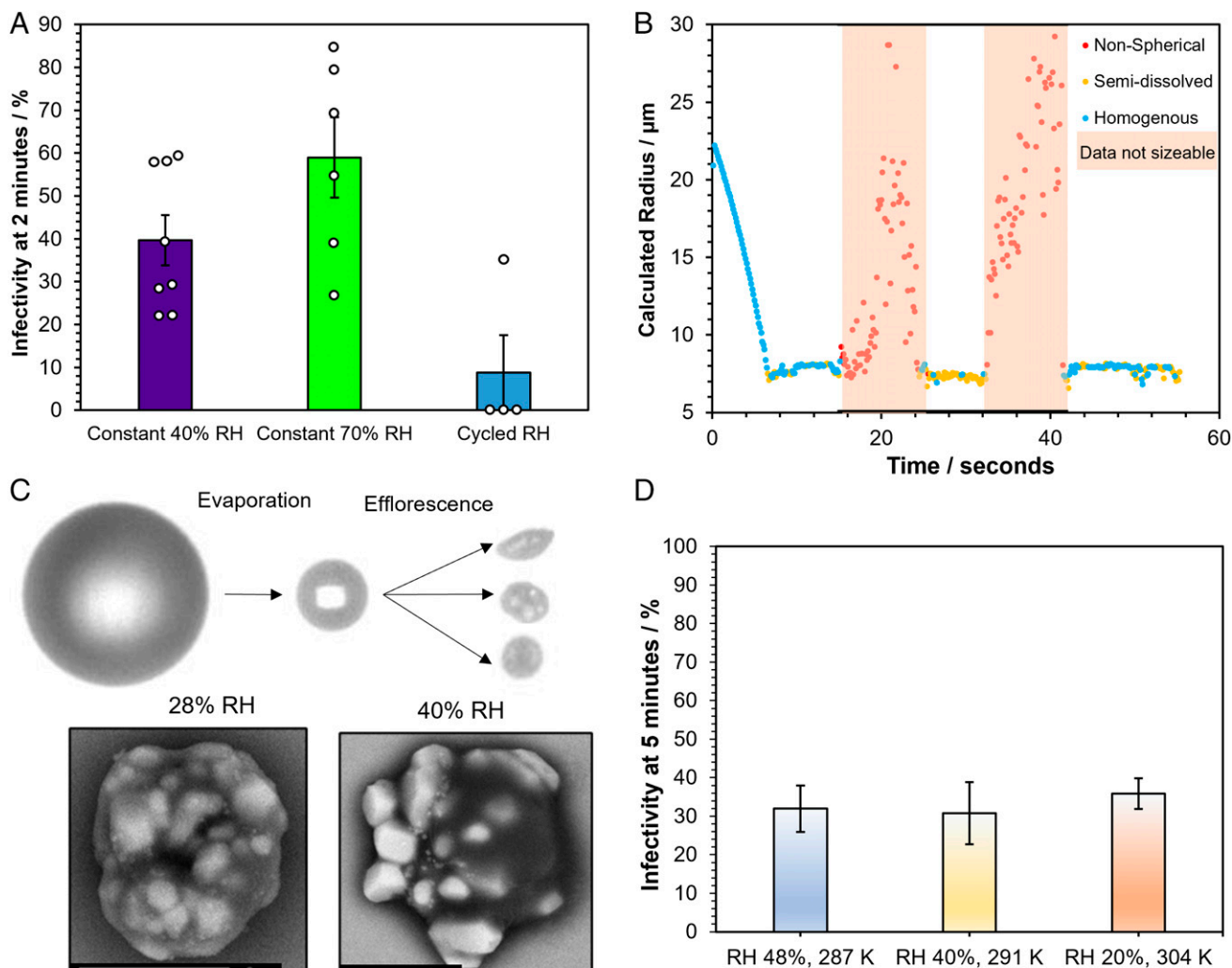


Fig. 3. The role of efflorescence in SARS-CoV-2 airborne loss of infectivity. (A) Comparison of the infectivity from Fig. 1B after 2-min levitations at constant 40% RH (purple bar) and 70% RH (green bar) with levitations where the RH has been cycled between 75 and 40% RH in one levitation (blue bar labelled cycled RH). The bars show the average % infectivity with error bars showing the standard error; the white circles show the % infectivity from the individual measurements. (B) CK-EDB measurements showing the phase behavior of levitated MEM droplets as the RH is cycled between 75 and 40%. RH is initially set at 75%, lowered to 40% at 14 s, raised to 75% at 24 s, lowered to 40% at 32 s, and finally raised to 75% at 41 s. Structural information about the droplet is denoted by the color of the data points as per Fig. 2A. (C) Images showing the changes in particle morphology that take place while MEM 2% FBS is airborne. The *Top* images are from the falling droplet column and showing the initial droplet generated by the dispenser on the *Left*, the droplet after 1.6 s of evaporation at 28% RH in the *Center*, and three different particles after they have undergone phase change on the *Right*. The *Bottom* shows two SEM images of droplets effloresced at 28% RH (*Left*) and 40% RH (*Right*). The scale bar is 5 μ m long. (D) Percent Infectivity of SARS-CoV-2 (REMRQ0001) measured after levitation for 5 min at three different temperatures and RHs. Bars show the mean of five measurements with error bars showing the standard error.

based on these measurements, it does not appear that the deletion in Bri Δ , or the array of mutations throughout B.1.1.7 and B.1.351, result in readily observable changes in the airborne longevity of the virus when compared with REMRQ0001. There is no reason to believe that the measurements in this study using REMRQ0001 are not representative of later-circulating variants of the virus.

Droplet pH, Carbon Dioxide Partitioning, and the Rate of the Loss of Infectivity at High RH. Replicating the physicochemical conditions that exist in the aerosol phase through bulk phase measurements is not possible except for conditions equivalent to the very highest RH. Under typical ambient conditions in the range 20 to 60% RH, solute concentrations are heavily supersaturated in equilibrated aerosols. In addition, the high surface-to-volume ratio in aerosol cannot be replicated, diminishing the potentially significant role of surface processes at the gas-liquid boundary and ignoring the influence of the rapid

microphysical dynamics including the coupling of heat and mass transfer. However, certain elements of the airborne change in droplet composition can be replicated in the bulk phase by simulating the concentrations of various components in the droplet at concentrations equivalent to equilibration at high RH. The steady concentrations of solutes when the aerosol is equilibrated at 90% RH are approximately a factor of 10 higher than in the starting droplets at a water activity of 0.995 (*SI Appendix, Fig. S4*), which is a concentration that can be replicated in the bulk. However, exposing SARS-CoV-2 to a 10-fold higher MEM concentration did not result in any observable loss of viral infectivity within 20 min (*SI Appendix, Fig. S7*). This suggests that this increased concentration of culture medium solutes is unable to account for the rate of the loss of infectivity in the aerosol phase.

In addition to changes in the concentration of solutes that occur on equilibration to the ambient RH, it is possible that the pH of aerosol droplets containing MEM can change

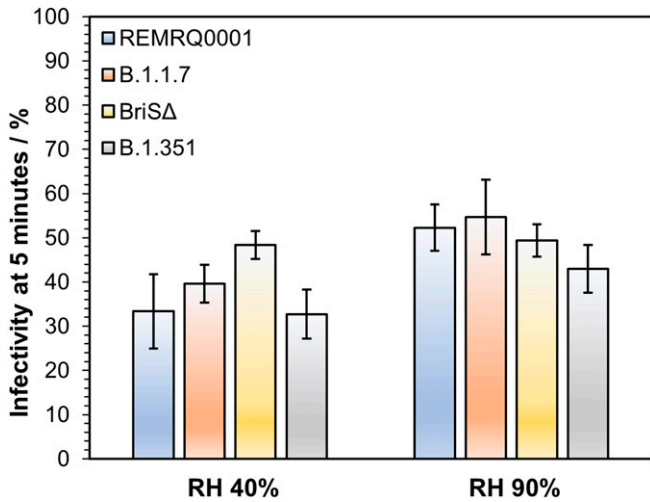
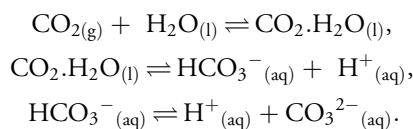


Fig. 4. The influence of SARS-CoV-2 strain on airborne stability. Infectivity of four different variants of SARS-CoV-2 (blue bars for REMRQ0001, orange bars for B.1.1.7, yellow bars for BriSΔ, gray bars for B.1.351). Infectivity is compared after 5 min of levitation at 40 and 90% RH, 18°C. At 40% RH, N = 5 for REMRQ0001, N = 8 for B.1.1.7, N = 4 for BriSΔ, and N = 10 for B.1.351. At 90% RH, N = 7 for REMRQ0001, N = 11 for B.1.1.7, N = 7 for BriSΔ, and N = 13 for B.1.351. Bars show the mean; error bars show the standard error.

rapidly. Although the sensitivity of SARS-CoV-2 infectivity both to high and to low pH has been reported (37, 64), these studies do not report measurements on a timescale relevant to the rapid loss of infectivity reported here in the aerosol phase. To investigate whether there is a loss of infectivity with the change in pH on a similar timescale, SARS-CoV-2 was suspended in tissue culture media at varying pH for 20 min, before dilution into neutral media and plating onto cells for infectivity quantification (*SI Appendix*, Fig. S8). Although no significant decrease in infectivity was observed after 20 min at pH ranging from 5.6 to 9, the average infectivity was diminished considerably above pH 9.5 so that only 7% of the virus remained infectious after 20 min at pH 11.2. The effect of pH was further explored by suspending SARS-CoV-2 in solutions of pH 9 and 11 for 30 min (Fig. 5A), with neutralization and quantification being carried out every 10 min. In this experiment, the virus remained stable in the pH 9 solution, but at pH 11, the infectivity fell to a similar level as in the 90% RH levitations, also seeming to plateau once 90% of the virus had been deactivated. These bulk phase studies suggest that the pH would have to increase to around 11 to explain the deactivation observed in the aerosol phase at 90% RH after 20 min. We therefore considered whether such a high pH could be present in the aerosol droplets at high RH conditions.

The equilibration between dissolved bicarbonate anions and gaseous CO₂ is particularly important to consider for many respiratory secretions as well as the tissue culture media often used in experimental studies of airborne viral survival (65). A set of coupled equilibria is established with a bicarbonate concentration that responds to changes in the level of gas phase CO₂, typically at an elevated gas phase concentration for cell culture and 50,000 ppmv in exhaled air, specifically,



Cell culture media typically contain 20 to 50 mM bicarbonate (50, 51) to buffer the aqueous solution at a pH ~7.4 when gas

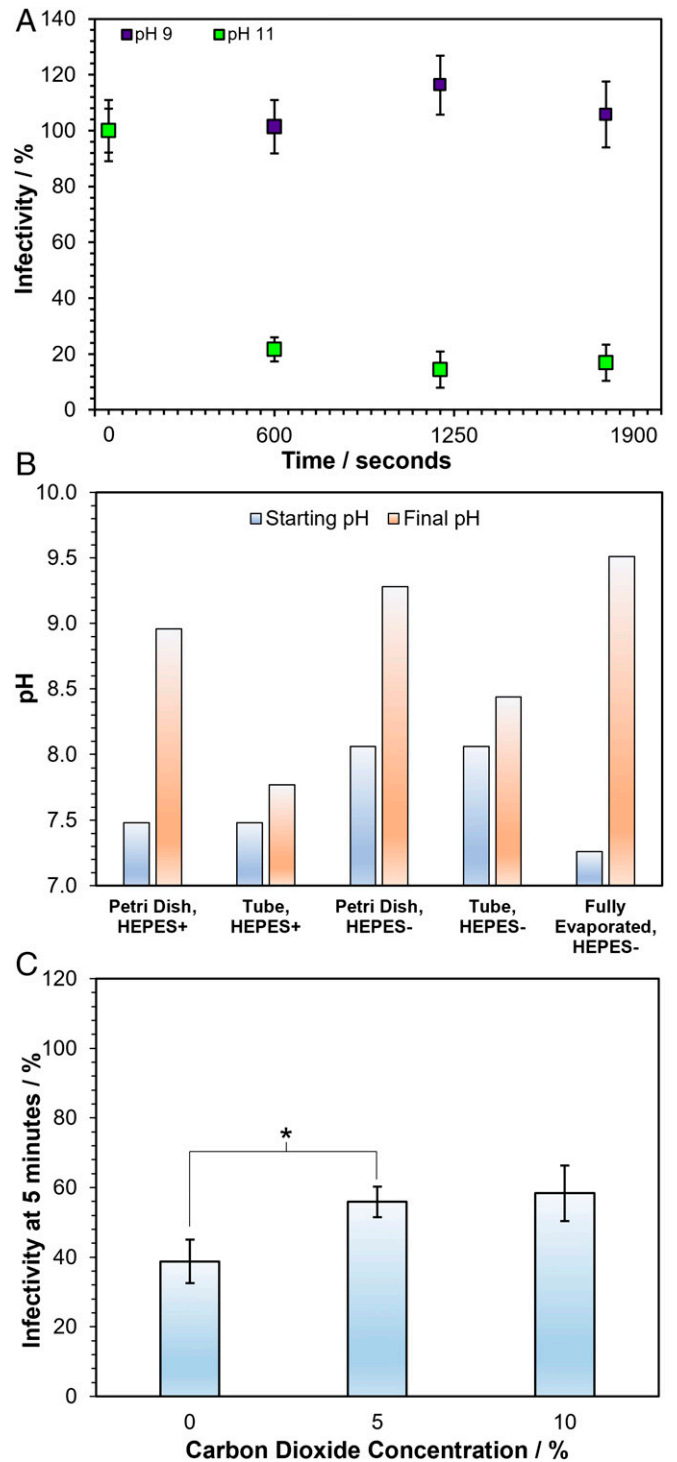


Fig. 5. The role of pH in SARS-CoV-2 airborne loss of infectivity. (A) Bulk % infectivity of SARS-CoV-2 (B.1.351) after a 30-min incubation in DMEM 2% FBS altered to either pH 9 (purple datapoints) or 11 (green datapoints), diluted back into neutral media and plated onto cells every 10 min. Datapoints are the mean of three measurements for pH 11 and five measurements for pH 9, with error bars showing the standard error. (B) The pH changes that tissue culture media (in this case DMEM) underwent when exposed to open air. DMEM was left in an open petri dish or 50-mL tube both with and without HEPES and the initial pH (blue bar) and the pH after 20 min (orange bar) was measured. The same measurement was carried out using thin layers of DMEM that were allowed to evaporate to 10% of their original volume over the course of 24 h (labelled fully evaporated). (C) The 5-min levitations were carried out with SARS-CoV-2 (B.1.351) at 90% RH with varying CO₂ concentrations mixed into the gas flow. Bars show the mean of 15 measurements for 0% CO₂, 16 measurements for 5% CO₂, and 6 measurements for 10% CO₂ with the error bars showing the standard error. **P* < 0.03 between 0% and 5% CO₂.

phase CO₂ is at an elevated concentration, 4 to 5% by volume. For bicarbonate in exhaled salivary aerosol (66), the lower gas phase CO₂ concentration in the environment after exhalation (0.04%) results in a change in the equilibrium concentration of bicarbonate in the aerosol by shifting the equilibria toward CO₂-H₂O_(l) and eventually CO_{2(g)}, leading to particle-to-gas phase partitioning of CO₂. Indeed, for laboratory studies of airborne survival, the aerosol is often generated in an environment devoid of CO₂, as is the case here, leading to irreversible evaporation of dissolved CO₂ into the gas phase. As evaporation occurs, the available H⁺ concentration diminishes, and the pH can be expected to rise.

As a bulk analog experiment, bulk tissue culture medium was exposed to ambient air for an extended time period (Fig. 5B). After 20 min in an open petri dish, the pH of DMEM (formulated with the same concentration of bicarbonate as the MEM used in the levitations) rises from 8 to 9.3. Adding HEPES reduces the initial pH of the medium, but the pH was still found to increase significantly after exposure to air, increasing from 7.4 to 9. When the DMEM solution was kept in an open 50-mL tube rather than a petri dish, decreasing the surface area for interaction, the rate of the rise in pH also decreased. A final experiment was carried out in which thin layers of DMEM were placed in petri dishes and allowed to evaporate to 10% of the starting volume over the course of 24 h, replicating both the CO₂ and H₂O equilibration that takes place in airborne droplets. The combination of CO₂ equilibration and volume loss resulted in the greatest pH rise, increasing from 7.25 to 9.5. The particle-gas partitioning can be expected to occur more rapidly than in any of these bulk examples because of facile transport across a droplet surface with a high surface-to-volume ratio. While the presence of bicarbonate buffers biological fluids such as saliva (66) when they are in the respiratory tract (or in a CO₂ supplied incubator), the decrease in the concentration of dissolved bicarbonate through the irreversible loss of CO₂ following their aerosolization will cause droplets to become more alkaline.

Sodium bicarbonate accounts for ~20% of the solute mass in MEM with ~65% sodium chloride by mass. With the loss of bicarbonate from MEM solution droplets, through irreversible evaporation of CO₂, the reduction in solute mass should lead to a reduction in the wet equilibrated size of the droplet with less solute able to sustain less water in the condensed phase. Indeed, it was possible to observe a long-time slow loss of CO₂ and dissolved solute using the CK-EDB for MEM solution droplets (*SI Appendix*, Fig. S9) and for mixtures of NaCl and NaHCO₃ (*SI Appendix*, Fig. S10), the two dominant salts. Droplets of both MEM and sodium bicarbonate continue to decrease in size for longer than the time required for the water activity to equilibrate to the gas phase RH. Indeed, the vapor pressures inferred from the data in *SI Appendix*, Fig. S10 with varying RH (0.0092, 0.014, and 0.052 Pa at 60, 75, and 90% RH) are consistent with calculations using the E-AIM model (www.aim.env.uea.ac.uk/aim/aim.php) (67) for the vapor pressure of CO₂ above supersaturated carbonate solutions at the same water activities (~0.01 Pa and increasing with increase in RH). By contrast, the vapor pressure of CO₂ from bicarbonate solutions at the same RHs are considerably higher (~100 kPa) and the particle-gas partitioning can be expected to occur extremely rapidly in <<1 s following aerosol droplet exhalation or generation, a process that can be expected to already be completed by the time the aerosol droplets are captured by CELEBS or the CK-EDB.

During the evaporation of water, as the moisture content of the aerosol equilibrates, the solutes surpass solubility limits for

various salts. The initial water activity of the starting droplets can be estimated as 0.9952 by considering the dominant ionic species alone (Na⁺, Ca²⁺, Cl⁻, and HCO₃⁻) using the E-AIM model (67). Calcium carbonate is particularly insoluble and becomes supersaturated from very early on in the evaporation process, successively followed by other binary and mixed salts, specifically CaNa₂(CO₃)₂·0.5H₂O(s), Na₂Ca(CO₃)₂·0.2H₂O(s), NaHCO₃(s), and finally NaCl(s) as water activity decreases. The droplet becomes saturated with respect to the first two salts above a water activity of 0.9, sodium bicarbonate at ~0.9, and NaCl below 0.8. Indeed, we observe the precipitation of salts during the droplet equilibration process as the water activity transitions through to the final equilibrated value, with significant supersaturation required for each before crystallization occurs (Fig. 2B). Until the crystallization of NaCl(s), which only occurs at the very lowest RHs of 50% and below, a partially deliquesced particle containing crystalline inclusions along with an aqueous phase leads to considerable variability in the remaining infectivity of the virus (Fig. 1B).

It can be hypothesized that increasing the concentration of CO_{2(g)} around the droplet would reduce the irreversible loss of bicarbonate from the droplet and could mitigate a pH-driven loss of infectivity. CO_{2(g)} was added to the airflow during CELEBS levitations at high RH and the infectivity of SARS-CoV-2 measured after 5 min (Fig. 5C). The elevation to a gas phase concentration of 5% by volume CO₂ (equivalent to 50,000 ppmv) around the droplet at 90% RH results in a small but significant increase in the remaining infectivity of SARS-CoV-2 after 5 min when compared with ambient CO_{2(g)} (0.04%). Increasing the steady CO_{2(g)} concentration around the trapped droplet cannot mitigate the loss of infectivity from pH changes during the initial travel of the droplet to the trapping region. While it is possible that elevated CO_{2(g)} around the droplet may have other physicochemical effects on the droplet in addition to decreasing the pH, this measurement provides further evidence that increased droplet pH is at least partly responsible for the observed falls in viral infectivity at high RH.

The influence of pH on infectivity is expected to be relevant in respiratory aerosols as the underlying physicochemical properties of exhaled aerosol (saliva) and MEM are similar, and numerous studies have demonstrated that exhaled breath condensate is alkaline (68–71). This dynamic is in stark contrast to environmental aerosols such as sea spray where, following generation, the pH of the sea spray droplets become more acidic through the uptake of acidic gases such as HCl and SO_x (72). Exhaled aerosol is generated in an environment with an extremely high concentration of an acidic gas (4 to 5% by volume CO₂) that can only be reduced once exhaled. This contrast in pH behavior following generation is clear when comparing studies of collected sea spray pH (72, 73) with those of collected exhaled breath condensate (69–71, 74). In short, while the vast majority of ambient aerosol may be acidic, exhaled aerosol can be expected to be alkaline. The pH of exhaled and model respiratory aerosols is an area in need of further study, with a need for measurements across a broad range of timescales, droplet compositions (saliva, sputum, MEM, DMEM), and environmental conditions (RH, [CO_{2(g)}]).

Comparison with Rotating Drum Studies of SARS-CoV-2. A motivation of our combined approach using CELEBS and CK-EDB is to identify the fundamental physicochemical parameters that dictate viral infectivity in the aerosol phase, progressing beyond general associations such as those between RH and infectivity, and to address the more challenging and informative questions allowing the identification of mechanistic

causation rather than just correlation. By taking this approach, it has been shown that SARS-CoV-2 undergoes a rapid deactivation in the first few minutes following droplet generation and that this deactivation occurs on efflorescence at low RH and possibly by an increase in droplet pH at high RH resulting from irreversible partitioning of CO₂ into the gas phase. There have been several reports of the aerostability of SARS-CoV-2 using the Goldberg rotating drum (14–16). However, given the relatively short timescale over which the majority of this deactivation occurs, which drum experiments cannot observe, and the importance of the physicochemical properties of the droplet in driving the deactivation, it is unsurprising that data collected from rotating drums report a longer lifetime for the virus in the aerosol phase.

Rotating drums have a poorly defined time-zero, meaning that the benchmark infectivity to which later time data are compared is poorly defined. The number of droplets suspended, their initial size, and viral units per droplet are both variable and uncontrolled and thus must be inferred offline. RH profiles, while they appear to be commonly collected in rotating drum experiments, are rarely reported in their entirety, with many drum studies only reporting a single RH value for each measurement (15). The location of the RH probe within the experiment, and whether the value is taken at a particular time or is an average across their experiment, is not always reported. Regardless, the RH recorded by a probe is likely unrelated to the RH trajectory that an aerosol droplet experiences as it passes from the nebulization source into the rotating vessel. Indeed, the nebulization of a cloud of aerosol at a high number concentration likely leads to some buffering of the RH in the gas phase, sustaining a higher value that would be typical of the very low respiratory aerosol concentrations actually generated (21). These uncertainties may make the influence of processes such as efflorescence on infectivity challenging to infer.

Comparisons of the time dependence and precision of the CELEBS measurements with those from rotating drum studies are reported in *SI Appendix, Figs. S11 and S12*. The time-resolution of the drum measurements make the initial decrease in infectivity challenging to identify. Indeed, the times of the indicated points (*SI Appendix, Fig. S11*) should not be taken as the time-resolution as discussed above. In addition, the average relative SD (RSD) from the CELEBS measurements is 0.37 (*SI Appendix, Fig. S12*), compared with 0.66 from van Doremalen et al. and 1.03 from Smither et al. (14) Two further papers do not report sufficient information to estimate RSDs (15, 16). The smaller RSD from the CELEBS is likely the result of the more stable environmental conditions, a more reproducible monodisperse droplet generation process, and improved methodology for viral infectivity quantification (39). Furthermore, CELEBS experiments are more straightforward to perform, allowing for more repeat measurements for each condition and leading to a high degree of confidence in the mean percentage infectivity values reported.

The nebulization of bicarbonate-buffered solutions into a confined volume results in the elevation of the CO₂ gas concentration (*SI Appendix, Fig. S13*). The magnitude of this elevation is dependent on many variables, including the pH of the nebulized solution, the nebulization time, and the drum volume. A survey of the literature failed to identify a single article where the CO₂ levels within a rotating drum was reported. As reported (*Fig. 5C*), CO₂ in the gas phase reduces the degradation of the virus likely by limiting the rise in droplet pH. CO₂ cannot be removed selectively during a rotating drum study, and the conditions likely support greater SARS-CoV-2

longevity. Accumulation of CO₂ is not an issue in CELEBS due to the constant flow of compositionally controlled air being maintained over the trapped droplets. In addition to potential issues with the pH of the airborne droplets in the rotating drum, it is also possible that the pH of the solution within the nebulizer may increase during the nebulization process (*SI Appendix, Fig. S14*), directly affecting the viral infectivity prior to nebulization (*Fig. 5A*).

Discussion

A combination of measurement strategies to probe the changes in airborne viral infectivity with time and the physicochemical transformation dynamics of the host aerosol is crucial to improve our understanding of the influence of environmental (such as RH, temperature) and biological (such as spike protein mutations) parameters on the transmission of viruses in the aerosol phase. While the current consensus is that the half-life of SARS-CoV-2 in the aerosol phase is between 1 and 2 h, if not longer, we report an initial rapid decline in infectivity within a few seconds to minutes of aerosol generation. Under all conditions measured, the majority of SARS-CoV-2 is inactivated within 10 min of aerosolization. Further research is required to determine for how long the remaining fraction persists, how this may depend on the viral load in the aerosol, and the influence of chemical composition. The high-time resolution infectivity measurements reported here are uniquely accessible to the CELEBS technology and can only be understood once the detailed aerosol microphysics are fully explored. Although we do not report measurements in artificial or real saliva, the culture media used do have many of the same characteristics of real respiratory secretions, particularly the high concentration of inorganic ions that dominate the phase behavior and water content of the aerosol, along with bicarbonate ions that partition CO₂ into the gas phase on aerosolization. In addition, the initial water activity of the aerosol is consistent with the high RH of the respiratory tract, and the aerosol generation process generates isolated droplets that must respond rapidly to the surrounding environmental conditions, which is typical of the very low concentrations of aerosol exhaled in infected individuals.

The aerostability data reported here are consistent with a view that the risk of SARS-CoV-2 transmission is greatest closer to the source of infection. Often, the assumption is that short distance transmission is caused by large droplets that fall to the ground more quickly and therefore do not travel as far. The rapid loss of infectivity demonstrated in these measurements provides an alternative explanation for a short transmission distance, with rapid airborne losses of viral infectivity possibly making transmission decreasingly likely as distance from the particle source is increased, even if the particles that contain the virus are small and able to travel long distances. This loss in infectivity is compounded by the considerable dilution in aerosol concentration that results following exhalation and transport beyond the short range. However, the rapid loss of infectivity must also be considered in combination with the large variability in aerosol emission rate between individuals [up to a factor of 10³ between individuals when breathing (75)] and viral titer in the exhaled aerosol [which could be as much as 10⁴ if variations in sampled saliva are indicative (76)].

We do not observe the characteristic “V-shape” relationship between RH and virus stability, where maximum virus loss occurs around RH = 50%. Rather, the largest loss of infectivity was observed at the lowest RHs. Previously, Goldberg drum

studies have not identified a strong dependence for SARS-CoV-2 survival on RH (14). However, following the initial loss of infectivity, the virus within the now dry particle appears to be somewhat stable when compared with the higher RH. Thus, if the initial rapid decrease in infectivity is not accounted for when reporting RH stability data, a V-shape relationship may be identifiable. However, not accounting for changes in viral infectivity that take place immediately after particle generation prevents the accurate coupling of airborne stability measurements with measurements of initial virus shedding, limiting the value of the V-shape relationship.

The rapid loss of SARS-CoV-2 infectivity through droplet efflorescence at an RH of <45% suggests that dry air may help to limit overall exposure. However, investigation of the impact that lowering RH has on particle transport in the exhalation jet is required to confirm this. The large impact of efflorescence on SARS-CoV-2 infectivity indicates that measuring the impact of environmental conditions on phase change in respiratory secretion aerosols may provide useful insights into COVID-19 transmission. Further research is needed to confirm with more certainty the degree to which pH is involved in the airborne loss of SARS-CoV-2 infectivity at high RH and to determine the exact mechanism by which the pH rise is deactivating the virus. The importance of elucidating the role of pH in the survival of SARS-CoV-2 in the aerosol phase cannot be understated. A literature survey found no manuscripts indicating that the alkaline nature of exhaled aerosol may affect viral infectivity. Contrarily, it has been reported that viruses may be inactivated by acid in the aerosol phase (77).

Elevation of CO₂ levels within a room is taken as a clear sign of occupancy and poor ventilation. There has been increasing discussion surrounding the use of CO₂ monitors as a means of determining the relative risk of COVID-19 transmission in various settings. The data from this study give further credence to this approach. Not only is elevated CO₂ an indication of a densely occupied, poorly ventilated space but it could also be indicative of an environment in which SARS-CoV-2 is more stable in the air. The precise elevation in CO₂ required for an observable increase in SARS-CoV-2 transmissibility is unknown and requires further investigation (5% CO₂ is not a concentration reached in typical indoor environments), but it is possible that this is an additional risk presented by poorly ventilated, densely occupied settings. If so, CO₂ monitors may present an immensely valuable means of assessing the relative risk of different indoor environments. Additionally, the apparent role of pH elevation in the deactivation of airborne virus suggests a currently unexplored role of condensable acid vapors, such as nitric acid (78, 79), in the role of infectivity. It is possible that the condensation of acidic components into exhaled aerosol may help to neutralize the initial rapid pH increase, lowering the pH and increasing the airborne stability of the virus.

The approach taken here has clearly demonstrated the value of a combined approach that considers both the aerosol microphysics and biological processes in tandem and on the same timescale, demonstrating that underlying parameters that drive SARS-CoV-2 inactivation in the aerosol phase are particle phase and pH. In further research, we intend to explore these processes over an even wider range of times, conditions, and virus variants. There also remain unanswered questions as to exactly how phase change and high pH deactivate the virus. Do these processes rupture the viral envelope or impart an irreversible modification to the spike

protein? Is the effect of pH the result of direct deprotonation of viral molecules or is it an indirect effect caused by alterations to the solubility of other components within the droplet? Answering such questions would provide key insights into the physicochemical and biomolecular processes governing SARS-CoV-2 transmission and airborne pathogen transmission more broadly. It is only by pushing the limits of aerobiology to this deeper level that we can hope to understand how best to prevent the airborne spread of disease.

Materials and Methods

Details of virus strains and methodologies for virus and cell culture, viral infectivity quantification, bulk stability measurements, CK-EDB measurements, and falling droplet column measurements can be found in *SI Appendix, Extended Materials and Methods*.

Generation and Trapping of Droplets. The reservoir of a droplet-on-demand dispenser (MicroFab) is filled with MEM 2% FBS. The application of a square waveform to the piezoelectric crystal results in a compression wave that passes through the dispenser's orifice and initiates the formation of a jet that forms droplets of uniform size with each pulse. A direct current voltage is applied to an induction electrode, positioned 2 to 3 mm from the dispenser tip, which leads to an ion imbalance in the jet, resulting in a droplet with a net charge (~5 fC). Using the Gouy-Chapman model (80), a salt containing droplets with this level of net charge can be predicted to have an electric field strength of 0 V/m throughout its core, with the outer most shell (with a depth of ~3 nm) having an electric field strength of 3 V/m. The presence of this net charge interacting with the electrodynamic field of the CELEBS/CK-EDB leads to confinement of the droplet within the null field point.

CELEBS Airborne Longevity Measurements. The environmental conditions were set by adjusting the Peltier voltage and polarity to set the temperature and the ratio of dry to wet air to set the humidity. SARS-CoV-2 suspension is drawn into a 1-mL syringe which is then attached to the instrument and used to feed the virus solution to the droplet dispenser via a remotely operated motor. Droplets are then generated and trapped as described above. Once the desired time is reached, an isolation plate is retracted causing the electric field to be set to zero; then, the droplets are pulled down into a plate containing 5 to 10 mL of DMEM 2% FBS so that the remaining virus can be quantified (*SI Appendix, Extended Materials and Methods*). For each measurement, two levitations are carried out. First, a short levitation of <5 s at 90% RH was used to measure the initial infectious unit per droplet number, and then a second levitation was used for which the droplets are kept in the trap for the conditions and length of time being investigated. Infectious units per droplet are normalized to the average of the short, high humidity levitations from that experiment, such that the levitation data can be presented as percentage infectivity.

Data Availability. The txt file data has been deposited in data.bris, the University of Bristol Research Data repository (81).

ACKNOWLEDGMENTS. This work was funded by the National Institute for Health Research-UK Research and Innovation (UKRI) rapid COVID-19 call, the Elizabeth Blackwell Institute for Health Research, the University of Bristol, and the Medical Research Council. Additionally, this work was supported by funding from the PROTECT COVID-19 National Core Study on transmission and environment, managed by the Health and Safety Executive on behalf of Her Majesty's Government. A.E.H. and M.O.-F. received funding from the Biotechnology and Biological Sciences Research Council, Project BB/T011688/1. A.D.D. is a member of the G2P-UK National Virology consortium funded by the Medical Research Council/UKRI (Grant MR/W005611/1) that supplied SARS-CoV-2 variants. H.P.O. is supported by funding from the Defence Science and Technology Laboratory and the Engineering and Physical Sciences Research Council. We also thank Robert Alexander for his contributions to discussions on aerosol pH.

1. T. Greenhalgh *et al.*, Ten scientific reasons in support of airborne transmission of SARS-CoV-2. *Lancet* **397**, 1603–1605 (2021).
2. S. Tang *et al.*, Aerosol transmission of SARS-CoV-2? Evidence, prevention and control. *Environ. Int.* **144**, 106039 (2020).
3. R. Turner, Covid-19 and aerosol transmission: Up in the air. *BMJ* **372**, n636 (2021).
4. World Health Organization, Transmission of SARS-CoV-2: Implications for infection prevention precautions. <https://www.who.int/news-room/commentaries/detail/transmission-of-sars-cov-2-implications-for-infection-prevention-precautions>. Accessed 19 May 2021..
5. L. Zhou, S. K. Ayeh, V. Chidambaram, P. C. Karakousis, Modes of transmission of SARS-CoV-2 and evidence for preventive behavioral interventions. *BMC Infect. Dis.* **21**, 496 (2021).
6. J. Cai *et al.*, Indirect virus transmission in cluster of COVID-19 cases, Wenzhou, China, 2020. *Emerg. Infect. Dis.* **26**, 1343–1345 (2020).
7. P. Azimi, Z. Keshavarz, J. G. Cedeno Laurent, B. Stephens, J. G. Allen, Mechanistic transmission modeling of COVID-19 on the *Diamond Princess* cruise ship demonstrates the importance of aerosol transmission. *Proc. Natl. Acad. Sci. U.S.A.* **118**, e2015482118 (2021).
8. J. A. Lednický *et al.*, Viable SARS-CoV-2 in the air of a hospital room with COVID-19 patients. *Int. J. Infect. Dis.* **100**, 476–482 (2020).
9. J. R. Port *et al.*, SARS-CoV-2 disease severity and transmission efficiency is increased for airborne compared to fomite exposure in Syrian hamsters. *Nat. Commun.* **12**, 4985 (2021).
10. CDC, Scientific brief: SARS-CoV-2 transmission. <https://www.cdc.gov/coronavirus/2019-ncov/science/science-briefs/sars-cov-2-transmission.html>. Accessed 21 September 2021.
11. S. Bae *et al.*, Epidemiological characteristics of COVID-19 outbreak at fitness centers in Cheonan, Korea. *J. Korean Med. Sci.* **35**, e288 (2020).
12. A. Brlek, S. Vidovič, S. Vuzem, K. Turk, Z. Simonovič, Possible indirect transmission of COVID-19 at a squash court, Slovenia, March 2020: Case report. *Epidemiol. Infect.* **148**, e120 (2020).
13. N. van Doremalen *et al.*, Aerosol and surface stability of SARS-CoV-2 as compared with SARS-CoV-1. *N. Engl. J. Med.* **382**, 1564–1567 (2020).
14. S. J. Smither, L. S. Eastaugh, J. S. Findlay, M. S. Lever, Experimental aerosol survival of SARS-CoV-2 in artificial saliva and tissue culture media at medium and high humidity. *Emerg. Microbes Infect.* **9**, 1415–1417 (2020).
15. A. C. Fears *et al.*, Comparative dynamic aerosol efficiencies of three emergent coronaviruses and the unusual persistence of SARS-CoV-2 in aerosol suspensions. medRxiv [Preprint] (2020). <https://doi.org/10.1101/2020.04.13.20063784>. Accessed 12 January 2021.
16. M. Schuit *et al.*, Airborne SARS-CoV-2 is rapidly inactivated by simulated sunlight. *J. Infect. Dis.* **222**, 564–571 (2020).
17. C. M. Sorensen, R. C. Flagan, U. Baltensperger, D. Y. H. Pui, Grand challenges for aerosol science and technology. *Aerosol Sci. Technol.* **53**, 731–734 (2019).
18. T. Santt-Temkiv *et al.*, Bioaerosol field measurements: Challenges and perspectives in outdoor studies. *Aerosol Sci. Technol.* **54**, 520–546 (2020).
19. L. Morawska *et al.*, Airborne particles in indoor environment of homes, schools, offices and aged care facilities: The main routes of exposure. *Environ. Int.* **108**, 75–83 (2017).
20. L. Bandiera *et al.*, Face coverings and respiratory tract droplet dispersion: Face covering effectiveness. *R. Soc. Open Sci.* **7**, 201663 (2020).
21. F. K. A. Gregson *et al.*, Comparing aerosol concentrations and particle size distributions generated by singing, speaking and breathing. *Aerosol Sci. Technol.* **55**, 681–691 (2021).
22. M. Alsved *et al.*, Exhaled respiratory particles during singing and talking. *Aerosol Sci. Technol.* **54**, 1245–1248 (2020).
23. R. S. Bradley, M. G. Evans, R. W. Whytlawgray, The rate of evaporation of droplets; evaporation and diffusion coefficients, and vapour pressures of dibutyl phthalate and butyl stearate. *Proc. R. Soc. Lond., A Contain. Pap. Math. Phys. Character* **186**, 368–390 (1946).
24. J. S. Walker *et al.*, Accurate representations of the microphysical processes occurring during the transport of exhaled aerosols and droplets. *ACS Cent. Sci.* **7**, 200–209 (2021).
25. A. Anselm, T. Heibel, J. Gebhart, G. Ferron, "In vivo"-studies of growth factors of sodium chloride particles in the human respiratory tract. *J. Aerosol Sci.* **21**, 427–430 (1990).
26. T. Oreszczyn, I. Ridley, S. H. Hong, P. Wilkinson, Mould and winter indoor relative humidity in low income households in England. *Indoor Built Environ.* **15**, 125–135 (2006).
27. S. M. Cornick, M. K. Kumaran, A comparison of empirical indoor relative humidity models with measured data. *J. Build. Phys.* **31**, 243–268 (2008).
28. B. E. Cummings, Y. Li, P. F. DeCarlo, M. Shiraiwa, M. S. Waring, Indoor aerosol water content and phase state in U.S. residences: Impacts of relative humidity, aerosol mass and composition, and mechanical system operation. *Environ. Sci. Process. Impacts* **22**, 2031–2057 (2020).
29. X. Y. Liu, Heterogeneous nucleation or homogeneous nucleation? *J. Chem. Phys.* **112**, 9949–9955 (2000).
30. X. Li, D. Gupta, H. J. Eom, H. K. Kim, C. U. Ro, Deliquescence and efflorescence behavior of individual NaCl and KCl mixture aerosol particles. *Atmos. Environ.* **82**, 36–43 (2014).
31. A. Peckhaus, S. Grass, L. Treuel, R. Zellner, Deliquescence and efflorescence behavior of ternary inorganic/organic/water aerosol particles. *J. Phys. Chem. A* **116**, 6199–6210 (2012).
32. R. J. Salo, D. O. Cliver, Effect of acid pH, salts, and temperature on the infectivity and physical integrity of enteroviruses. *Arch. Virol.* **52**, 269–282 (1976).
33. N. J. Dimmock, Differences between the thermal inactivation of picornaviruses at "high" and "low" temperatures. *Virology* **31**, 338–353 (1967).
34. H. Wei *et al.*, Aerosol microdroplets exhibit a stable pH gradient. *Proc. Natl. Acad. Sci. U.S.A.* **115**, 7272–7277 (2018).
35. K. Lin, C. R. Schulte, L. C. Marr, Survival of MS2 and $\phi 6$ viruses in droplets as a function of relative humidity, pH, and salt, protein, and surfactant concentrations. *PLoS One* **15**, e0243505 (2020).
36. L. J. Goldberg, H. M. S. Watkins, E. E. Boerke, M. A. Chatigny, The use of a rotating drum for the study of aerosols over extended periods of time. *Am. J. Hyg.* **68**, 85–93 (1958).
37. M. E. R. Darnell, K. Subbarao, S. M. Feinstone, D. R. Taylor, Inactivation of the coronavirus that induces severe acute respiratory syndrome, SARS-CoV. *J. Virol. Methods* **121**, 85–91 (2004).
38. M. O. Fernandez, R. J. Thomas, H. Oswin, A. E. Haddrell, J. P. Reid, Transformative approach to investigate the microphysical factors influencing airborne transmission of pathogens. *Appl. Environ. Microbiol.* **86**, e01543-20 (2020).
39. H. P. Oswin *et al.*, Measuring stability of virus in aerosols under varying environmental conditions. *Aerosol Sci. Technol.* **55**, 1315–1320 (2021).
40. M. O. Fernandez *et al.*, Assessing the airborne survival of bacteria in populations of aerosol droplets with a novel technology. *J. R. Soc. Interface* **16**, 20180779 (2019).
41. A. Marsh, G. Rovelli, R. E. H. Miles, J. P. Reid, Complexity of measuring and representing the hygroscopicity of mixed component aerosol. *J. Phys. Chem. A* **123**, 1648–1660 (2019).
42. A. Marsh *et al.*, Influence of organic compound functionality on aerosol hygroscopicity: Dicarboxylic acids, alkyl-substituents, sugars and amino acids. *Atmos. Chem. Phys.* **17**, 5583–5599 (2017).
43. Y. Y. Su, A. Marsh, A. E. Haddrell, Z. M. Li, J. P. Reid, Evaporation kinetics of polyol droplets: Determination of evaporation coefficients and diffusion constants. *J. Geophys. Res. Atmos.* **122**, 12317–12334 (2017).
44. S. S. Steimer *et al.*, Electrodynamic balance measurements of thermodynamic, kinetic, and optical aerosol properties inaccessible to bulk methods. *Atmos. Meas. Tech.* **8**, 2397–2408 (2015).
45. C. Marcolli, U. K. Krieger, Phase changes during hygroscopic cycles of mixed organic/inorganic model systems of tropospheric aerosols. *J. Phys. Chem. A* **110**, 1881–1893 (2006).
46. A. Haddrell, G. Rovelli, D. Lewis, T. Church, J. Reid, Identifying time-dependent changes in the morphology of an individual aerosol particle from its light scattering pattern. *Aerosol Sci. Technol.* **53**, 1334–1351 (2019).
47. N. S. Ogando *et al.*, SARS-coronavirus-2 replication in Vero E6 cells: Replication kinetics, rapid adaptation and cytopathology. *J. Gen. Virol.* **101**, 925–940 (2020).
48. B. Kallapur *et al.*, Quantitative estimation of sodium, potassium and total protein in saliva of diabetic smokers and nonsmokers: A novel study. *J. Nat. Sci. Biol. Med.* **4**, 341–345 (2013).
49. H. H. Chauncey *et al.*, Composition of human saliva. Parotid gland secretory rate and electrolyte concentration in children with cystic fibrosis. *Arch. Oral Biol.* **7**, 707–713 (1962).
50. J. A. Hildes, M. H. Ferguson, The concentration of electrolytes in normal human saliva. *Can. J. Biochem. Physiol.* **33**, 217–225 (1955).
51. J. A. Young, C. A. Schneyer, Composition of saliva in mammalia. *Aust. J. Exp. Biol. Med. Sci.* **59**, 1–53 (1981).
52. G. B. Proctor, A. M. Shaalan, Disease-induced changes in salivary gland function and the composition of saliva. *J. Dent. Res.* **100**, 1201–1209 (2021).
53. J. K. M. Aps, L. C. Martens, Review: The physiology of saliva and transfer of drugs into saliva. *Forensic Sci. Int.* **150**, 119–131 (2005).
54. Y. Li, X. X. Tang, Abnormal airway mucus secretion induced by virus infection. *Front. Immunol.* **12**, 701443 (2021).
55. R. Vehring, W. R. Foss, D. Lechuga-Ballesteros, Particle formation in spray drying. *J. Aerosol Sci.* **38**, 728–746 (2007).
56. R. Vehring, Pharmaceutical particle engineering via spray drying. *Pharm. Res.* **25**, 999–1022 (2008).
57. L. E. Bockstahler, P. Kaesberg, The molecular weight and other biophysical properties of Bromegrass mosaic virus. *Biophys. J.* **2**, 1–9 (1962).
58. A. G. Murray, G. A. Jackson, Viral dynamics: A model of the effects of size, shape, motion and abundance of single-celled planktonic organisms and other particles. *Mar. Ecol. Prog. Ser.* **89**, 103–116 (1992).
59. J. Archer, J. S. Walker, F. K. A. Gregson, D. A. Hardy, J. P. Reid, Drying kinetics and particle formation from dilute colloidal suspensions in aerosol droplets. *Langmuir* **36**, 12481–12493 (2020).
60. F. K. A. Gregson, J. F. Robinson, R. E. H. Miles, C. P. Royall, J. P. Reid, Drying kinetics of salt solution droplets: Water evaporation rates and crystallization. *J. Phys. Chem. B* **123**, 266–276 (2019).
61. D. A. Hardy *et al.*, High time resolution measurements of droplet evaporation kinetics and particle crystallisation. *Phys. Chem. Chem. Phys.* **23**, 18568–18579 (2021).
62. A. D. Davidson *et al.*, Characterisation of the transcriptome and proteome of SARS-CoV-2 reveals a cell passage induced in-frame deletion of the furin-like cleavage site from the spike glycoprotein. *Genome Med.* **12**, 68 (2020).
63. J. L. Daly *et al.*, Neuropilin-1 is a host factor for SARS-CoV-2 infection. *Science* **370**, 861–865 (2020).
64. K. H. Chan *et al.*, Factors affecting stability and infectivity of SARS-CoV-2. *J. Hosp. Infect.* **106**, 226–231 (2020).
65. R. I. Freshney, *Culture of Animal Cells: A Manual of Basic Technique and Specialized Applications* (John Wiley & Sons, 2015).
66. A. Bardow, D. Moe, B. Nyvad, B. Nauntofte, The buffer capacity and buffer systems of human whole saliva measured without loss of CO₂. *Arch. Oral Biol.* **45**, 1–12 (2000).
67. A. S. Wexler, S. L. Clegg, Atmospheric aerosol models for systems including the ions H⁺, NH₄⁺, Na⁺, SO₄²⁻, NO₃⁻, Cl⁻, Br⁻, and H₂O. *J. Geophys. Res.* **107**, 4207 (2002).
68. M. Riediker, B. Danuser, Exhaled breath condensate pH is increased after moderate exercise. *J. Aerosol Med.* **20**, 13–18 (2007).
69. S. Svensson, J. Hellgren, pH in nasal exhaled breath condensate in healthy adults. *Rhinology* **45**, 214–217 (2007).
70. I. Horváth *et al.*, ATS/ERS Task Force on Exhaled Breath Condensate, Exhaled breath condensate: Methodological recommendations and unresolved questions. *Eur. Respir. J.* **26**, 523–548 (2005).
71. B. R. Winters *et al.*, Standardization of the collection of exhaled breath condensate and exhaled breath aerosol using a feedback regulated sampling device. *J. Breath Res.* **11**, 047107 (2017).
72. K. J. Angle *et al.*, Acidity across the interface from the ocean surface to sea spray aerosol. *Proc. Natl. Acad. Sci. U.S.A.* **118**, e2018397118 (2021).
73. W. C. Keene, A. A. P. Pszenny, J. R. Maben, R. Sander, Variation of marine aerosol acidity with particle size. *Geophys. Res. Lett.* **29**, 5–1–5–4 (2002).
74. E. Marek, P. Platen, J. Volke, K. Mückenhoff, W. Marek, Hydrogen peroxide release and acid-base status in exhaled breath condensate at rest and after maximal exercise in young, healthy subjects. *Eur. J. Med. Res.* **14** (suppl. 4), 134–139 (2009).
75. J. Archer *et al.*, Comparing aerosol number and mass exhalation rates from children and adults during breathing, speaking and singing. *Interface Focus* **12**, 20210078 (2022).
76. O. O. Adeniyai *et al.*, Infectious severe acute respiratory syndrome coronavirus 2 (SARS-CoV-2) in exhaled aerosols and efficacy of masks during early mild infection. *Clin. Infect. Dis.* **2**, ciab797 (2021).
77. W. Yang, L. C. Marr, Mechanisms by which ambient humidity may affect viruses in aerosols. *Appl. Environ. Microbiol.* **78**, 6781–6788 (2012).
78. L. Liu *et al.*, The role of nitric acid in atmospheric new particle formation. *Phys. Chem. Chem. Phys.* **20**, 17406–17414 (2018).
79. A. P. Ault *et al.*, Heterogeneous reactivity of nitric acid with nascent sea spray aerosol: Large differences observed between and within individual particles. *J. Phys. Chem. Lett.* **5**, 2493–2500 (2014).
80. C. F. Chamberlayne, R. N. Zare, Simple model for the electric field and spatial distribution of ions in a microdroplet. *J. Chem. Phys.* **152**, 184702 (2020).
81. J. Reid, A. Haddrell, M. O. Fernandez, H. Oswin, SARS-CoV-2 survival. data.bris.10.5523/bris.y4uo5scfqwan2gnthu1eyq7g0. Deposited 30 May 2022.